

Phase Transformation Path in Aluminum Under Ramp Compression; Simulation and Experimental Study

Lijie He

University of Rochester

Danae Polsin

University of Rochester

Shuai Zhang

University of Rochester

Gilbert W. Collins

University of Rochester

Niaz Abdolrahim (✉ niaz@rochester.edu)

University of Rochester

Research Article

Keywords: Phase transformation path, Aluminum, ramp compression, simulation, experimental study, plastic deformation, experimental observation, great accuracy

Posted Date: November 3rd, 2021

DOI: <https://doi.org/10.21203/rs.3.rs-1024584/v1>

License:  This work is licensed under a Creative Commons Attribution 4.0 International License.

[Read Full License](#)

Phase transformation path in Aluminum under ramp compression; simulation and experimental study

Lijie He¹, Danae Polsin^{2,3}, Shuai Zhang³, Gilbert W. Collins^{2,3,4}, Niaz Abdolrahim*^{1,2}

1. Materials Science Program, University of Rochester, Rochester, NY 14627, USA
2. Departments of Mechanical Engineering, University of Rochester, Rochester, NY 14627, USA
3. Laboratory for Laser Energetics, University of Rochester, Rochester, NY 14623, USA
4. Department of Physics and Astronomy, University of Rochester, Rochester, NY 14627, USA

Abstract

Identifying structure phase transformation path is essential but challenging in plastic deformation under high-pressure high-strain rate experiments. In this paper, we adopt a framework based on non-equilibrium molecular dynamics and virtual diffraction to reproduce the phase transformation event observed in laser-driven ramp compression. Our simulation results reveal the detailed phase transformation pathway with atomic-level deformation physics while the simulated stress-density response and virtual diffraction patterns match the experimental observation with great accuracy.

Introduction

The advancement in experimental techniques has drastically improved our understanding of the solid-phase stability and solid-solid phase transformation under high pressure. The development of gas gun¹, pulsed-power², and laser drivers³, combined with *in-situ* x-ray diffraction (XRD)^{4,5}, unveiled structure deformation mechanisms of numerous materials under dynamic, high-pressure quasi-isentropic compression with strain rates ranging from 10^4 - 10^8 s⁻¹. While the signatures of various phases and defects have been identified, determining the exact phase transformation pathway from experiments is still challenging⁶. This is when the employment of the computational methods becomes advantageous, which can determine the deformation path on the atomistic level, investigate the presence and contribution of defects, and provide validating evidence to be compared with the experiment. Non-equilibrium molecular dynamics (NEMD) is such a tool that is suitable for studying irreversible macroscopic processes according to the second law of thermodynamics, such as spallation⁷, shock loading⁸, and ramp loading^{9,10}. Previous work by Thompson et al.¹¹, as well as Lane et al.⁹, have demonstrated that NEMD in a reduced system is fully capable of capturing all of the elastic and most of the plastic response during ramp loading of a much larger system, providing that the time and position are scaled by the same factor while compression rate dx/dt is held constant. This theory enabled computational investigation of ramp-compression experiments on the spatial and temporal dimensions of microns and nanoseconds to be conducted in a reduced system on the scale of nanometers and picoseconds, which is approachable by NEMD simulation. With the benefit of knowing the exact atomistic configuration of the structure at each stage during NEMD simulation of ramp loading, virtual XRD and select-area-electron-diffraction (SAED)¹² profiles can be easily obtained and compared with experiments. Thus, NEMD simulations will provide fundamental understanding of the plastic deformation mechanisms and structural phase transformation pathway.

In this manuscript, we will use NEMD simulations with dynamic scaling to study phase transformations of ramp compressed Aluminum. We will then revisit our previous findings of the structural phase transformation mechanism of Aluminum, where it undergoes face-centered cubic (fcc) to body-centered cubic (bcc) phase transitions under laser-driven ramp compression with *in-situ* XRD^{6,13}. We first investigate the stress-density response by using different temporal and spatial scaling factors. When the simulation adopts the same scaling factor for both temporal and spatial dimensions comparing to the experiment (e.g., 1/20 of the experiment), the stress-density matches the experimental observations. Then, based on the XRD and SAED pattern analysis, atomistic snapshots analysis, and local lattice orientation calculation, we discuss the structural phase transformation path featuring a dislocation-assisted Bain transformation, which differs from the previous prediction. Finally, the virtual XRD and SAED of the structure at the different stages are compared with the experimental observation, showing a striking agreement in the experimental fcc and bcc aluminum XRD patterns at high pressures.

Although MD simulations have the advantage of accurately representing atomic-level deformation physics, they have the critical drawback of only applying to systems with a limited temporal/spatial scale due to the high computational cost¹⁴. This drawback is even more prominent in ramp loading studies, where the experimental strain rate is slow (less than $10^6/s$). In order to achieve lower ramp rates in MD, longer simulation durations are required. In turn, larger systems are also needed to allow stress wave development and propagation. These limitations put a heavy burden on the computational cost, justifying the need to reduce the system size without compromising the capability to predict the physics of deformation. Thus, dynamic scaling of the ramp loading system has been proposed and scrutinized^{9, 11} to overcome this problem. Details of

the method are as follows: assuming one-dimensional flow, the piston trajectory can be scaled linearly in both coordination and time by a factor of $1/M$:

$$x_s(t_s) = \frac{1}{M}x(t)$$

$$t_s = \frac{1}{M}t$$

where x denotes coordination, t denotes time; variables with subscript s indicate scaled values.

Doing such will ensure the piston velocity under the scaled coordination remains the same:

$$v_s(t_s) = \frac{\partial x_s}{\partial t_s} = \frac{\frac{1}{M}\partial x}{\frac{1}{M}\partial t} = \frac{\partial x}{\partial t} = v(t)$$

The ratio between the forces of the scaled system and the original system satisfies:

$$\frac{F_s}{F} = \frac{m_s(L_s/T_s^2)}{m(L/T^2)} = \frac{\rho_s A_s L_s (L_s/T_s^2)}{\rho A L (L/T^2)} = \left(\frac{\rho_s}{\rho}\right) \left(\frac{L_s}{L}\right)^2 \left(\frac{T_s}{T}\right)^{-2}$$

where m, L, T, ρ, A denotes mass, length, time, density, and cross-section area. Since the scaling only happens on one dimension,

$$A_s = A$$

The ratio between scaled and original length, time, and density can be acquired through equation

(1):

$$\frac{L_s}{L} = \frac{T_s}{T} = \frac{1}{M}$$

$$\frac{\rho_s}{\rho} = 1$$

plugging into equation (4),

$$\frac{F_s}{F} = 1$$

which suggests the forces are invariant to the proposed scaling. As a result, no modification towards the interatomic potential is needed. Similarly, velocity, strain, stress, density, and temperature are all invariant to the proposed scaling. On the contrary, acceleration, strain rate, and any extensive variable are not invariant. The scaling method is only valid when the spatial and temporal scaling parameters are equal. A dimensionless strain rate $\dot{\tilde{v}}_p$ is proposed by Lane et al.⁹, to identify systems that satisfy this prerequisite:

$$\dot{\tilde{v}}_p = \frac{v_t L}{\tau C_0^2}$$

where $v_t = 6 \text{ km/s}$ is the terminal velocity for both the experiment and the simulation. τ denotes the acceleration duration, L is the piston length and $C_0 = 6.27 \text{ km/s}$ is the ambient sound velocity of Aluminum. According to the scaling method, setups with the same dimensionless strain rate have identical temporal and spatial scaling factors and thus satisfy the scaling prerequisite. It is worth pointing out the scaling method also has certain limitations: first, it only works well under quasi-one-dimensional simulation setups. Changes in the lateral dimensions could potentially destroy the invariance of force and introduce significant errors. Second, it is proven by Thompson et al.¹¹ that the scaling method does not strictly apply to the plastic regime, especially when the overall system size is too small to produce reliable statistics. Nevertheless, they reported excellent scaling in the plastic regime, suggesting that the scaling method could be viable, but system size and plastic deformation must be carefully considered. To verify the scaling method, we have conducted multiple ramp-loading molecular simulations on different <001>-oriented single-crystal (SC) and texturized nanocrystalline (NC) with different scaling factors, as summarized in table 1. For each SC setup, an initial <001>-oriented SC Al system with varying sizes is created and ramp compressed in Z direction; pistons are set initially at the lower Z boundary and move up with linearly increasing velocity up to 6 km/s.

However, the acceleration duration is different for each setup. Periodic boundary conditions are applied along transverse directions. A momentum mirror that reflects the momentum of any atom, that comes in contact with it, is applied at the higher Z boundary. The lateral size (along transverse direction x and y) in SC models is set at 10.12 *nm*, while the length (along the loading direction z) varies from 100 *nm* to 2 *microns*. The deformation behaviors of different setups are discussed in details in the results section. Furthermore, a structure with the same setting as setup II except for three times larger lateral size (30.37 *nm*) has also been tested and compared with setup II. No difference was observed in their macroscopic mechanical response and microscopic deformation mechanisms, indicating that the structure dimension is large enough to produce reliable and consistent results. The texturized NC structure is generated via Voronoi tessellation¹⁵. In order to allow dislocations to pile up and interact with each other in the nanograins, the average grain size is set to be 15 nm, and subsequently, the structure dimension is set at 30.37 nm×30.37 nm×100 nm with a total atom count of 5.6×10^6 . Thus, the acceleration duration is set at 50 picoseconds (ps) to fulfill a scaling factor of 1/200 for both time and length, which is the same as setup I. Detailed discussion on the behavior of texturized NC structure is provided in section 6.

Results and discussion

1. Stress-density response and atomistic deformation path

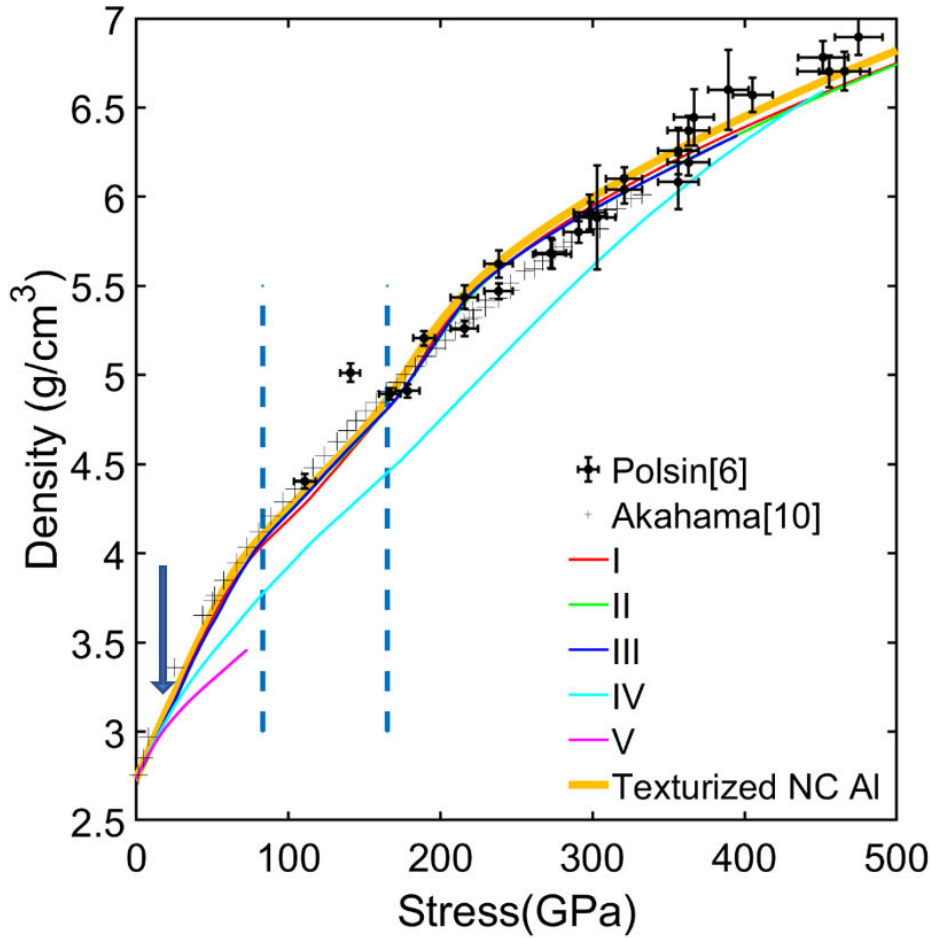


Figure 1 Density–stress curves for different simulation setups. The data are compared with ramp experiment from Ref [6] and DAC data from Ref [10]. Blue arrow indicates the deviation point between setups I, II, III and IV, V, at which the elastic wave reached the backend of the structure and was reflected in setups I, II, and III. The first vertical dashed bar denotes the pressure onset for 100% bcc in setups II and III. In between the two vertical dashed bars, the structure is full bcc and deforming elastically for setup II and III. After the second dashed bars, defect growth is observed in setup II and III. For setup I, 100% bcc is triggered at a lower stress, causing the curve to deviate from setups II and III in between the two vertical bars.

Table 1 Experiment and simulation setups. Within the duration of each, the piston velocity linearly ramps from zero up to 6 km/s.

Setup	Length(nm)	Duration (ps)	Length Scale Factor	Time Scale Factor	Atom Count	Dimensionless strain rate
Polsin (Experiment)	20000	10000	1	1	N/A	0.306
I	100	50	1/200	1/200	6.25×10^5	0.306
II	1000	500	1/20	1/20	6.25×10^6	0.306
III	2000	1000	1/10	1/10	1.25×10^7	0.306
IV	1000	250	1/20	1/40	6.25×10^6	0.612
V	2000	250	1/10	1/40	1.25×10^7	1.224
Texturized NC	100	50	1/200	1/200	$5.63 \times 10^{6*}$	0.306

* The texturized NC structure possess a larger lateral size, thus having disproportional large atom count.

In this section, the stress-density response and deformation behaviors of all SC setups are discussed and compared in detail. As illustrated in Table 1, setups I, II, and III have the same dimensionless strain rate as the experimental setup (i.e., the length and time scale factor are equal for each setup). In contrast, setup IV and V possess larger dimensionless strain rates. As shown in Figure 1, the stress-density curves of setups I, II, and III are in very good agreement with experiments, while setups IV and V are deviated from the experimental results due to having incompatible temporal and spatial scaling factors. Closer inspection reveals that at the deviation point (indicated by the blue arrow in Figure 1), the elastic wave reached the backend of the structure and was reflected in setups I, II, and III. The reflected wave interacted with the forward propagating wave and reduced the global stress in the structures. A similar mechanism also occurs in the experiments. The Al sample is tamped by a LiF window resulting in a partial reflection of the elastic wave that occurs at the interface, although the Al and LiF are well impedance matched. In comparison, the elastic wave was still propagating forward in setup IV and V at this point. As a consequence, the pressure continued to increase and deviated from other setups and experiments.

Figure 2 shows a series of snapshots of a centerpiece from setup II at different times. The structure goes through the following stages. From 0 GPa to 10 GPa, this piece goes through elastic deformation. At 14 GPa, micro twin faults (i.e., thin twin faults with only 3-4 atomic layers) form along the (111) slip plane. At 28 GPa, new leading Shockley partials start to nucleate and propagate, leaving stacking faults (SFs) along the $(\bar{1}\bar{1}1)$ planes behind. When these $(\bar{1}\bar{1}1)$ SFs intersect with the (111) micro twins; the micro twins get unzipped and transform into (111) SFs. With further ramp compressing, the (111) SFs thicken until around 65 GPa, when bcc aluminum starts to nucleate in certain parts of the structure. The bcc phase first nucleates at

or in the vicinity of the intersecting SFs on $(\bar{1}11)$ and (111) slip planes, see the illustration in the magnified circle in Figure 2. This mechanism for new bcc phase nucleation is similar to the Olson-Cohen model¹⁶ that describes the austenite to α' -martensite phase transformation facilitated by the SFs observed in iron-based alloy¹⁷⁻¹⁹. The bcc phase then proliferates, surpasses SFs thickening, and becomes the dominant mechanism at around 80 GPa. At around 90 GPa, the structure fully transforms into bcc. The nature of this phase transformation will be discussed in detail in section 4. After the phase transformation, the structure deformed elastically from 90 GPa to 165 GPa, corresponding to the linear response at a reduced slope in the stress-density curves (between the blue dotted line). Then as defects start to nucleate in the bcc phase above 165 GPa, the stress-density curve changes slope again.

For setup I with a smaller scaling factor (1/200), albeit the stress-density curve is very similar to setup II and III, discrepancies in mechanical behavior start to manifest as soon as plasticity starts. Instead of micro twin activation on only one slip plane, plasticity initiated by activation of SFs on multiple slip planes setup I. The phase transformation is also triggered and complete at smaller stresses; the entire structure transformed to bcc at 76 GPa, compared to 113 GPa for the larger scale factors (setup II and III). Furthermore, the new bcc phase in setup I exhibits a non-negligible amount of point defects (a minimum of 3.6% of the atoms at 102 GPa and keep increasing); in comparison, the bcc phase in setups II and III was almost defect-free (<0.1% atoms) from 100 GPa to 165 GPa. This difference in the bcc phase behavior leads to a subtle deviation in the density-pressure curves between the aforementioned stress range, as illustrated in Figure 1. Thus, it is concluded the scaling method is not accurate with a scaling factor of 1/200 (setup I). Thompson et al.¹¹ have also observed similar behavior and concluded that finite system size effects in plastic regimes could invalidate the scaling method and conclude that

making the system larger could mitigate this issue. Indeed, Setup II (scaling factor 1/20) behaves identically as setup III (scaling factor 1/10) during the entire loading process, indicating a scaling factor of 1/20 is sufficient for the prediction of proper plastic deformation behavior using the scaling method. As a balance between model accuracy and computational efficiency, setup II will be the focus of this investigation.

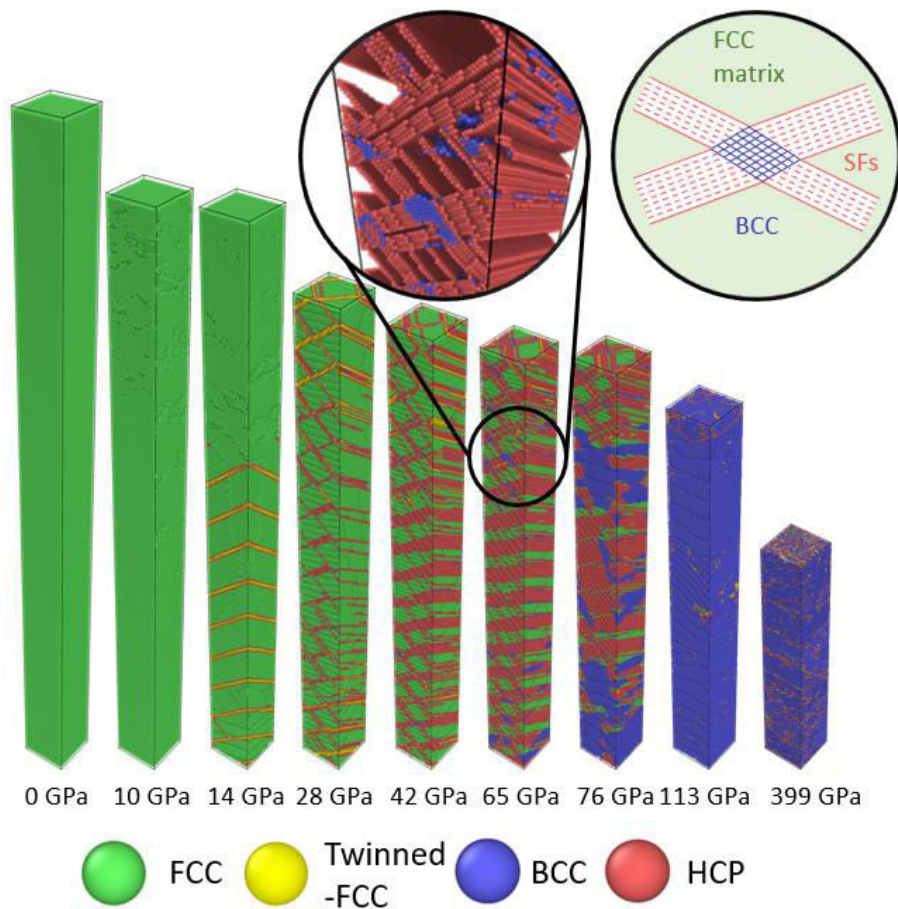


Figure 2 Atomistic snapshot of a representative slice from setup II at different global stress states. The loading direction is from bottom to top. The magnification of the circled area shows the initial bcc nucleation, where fcc atoms are not displayed for clarity.

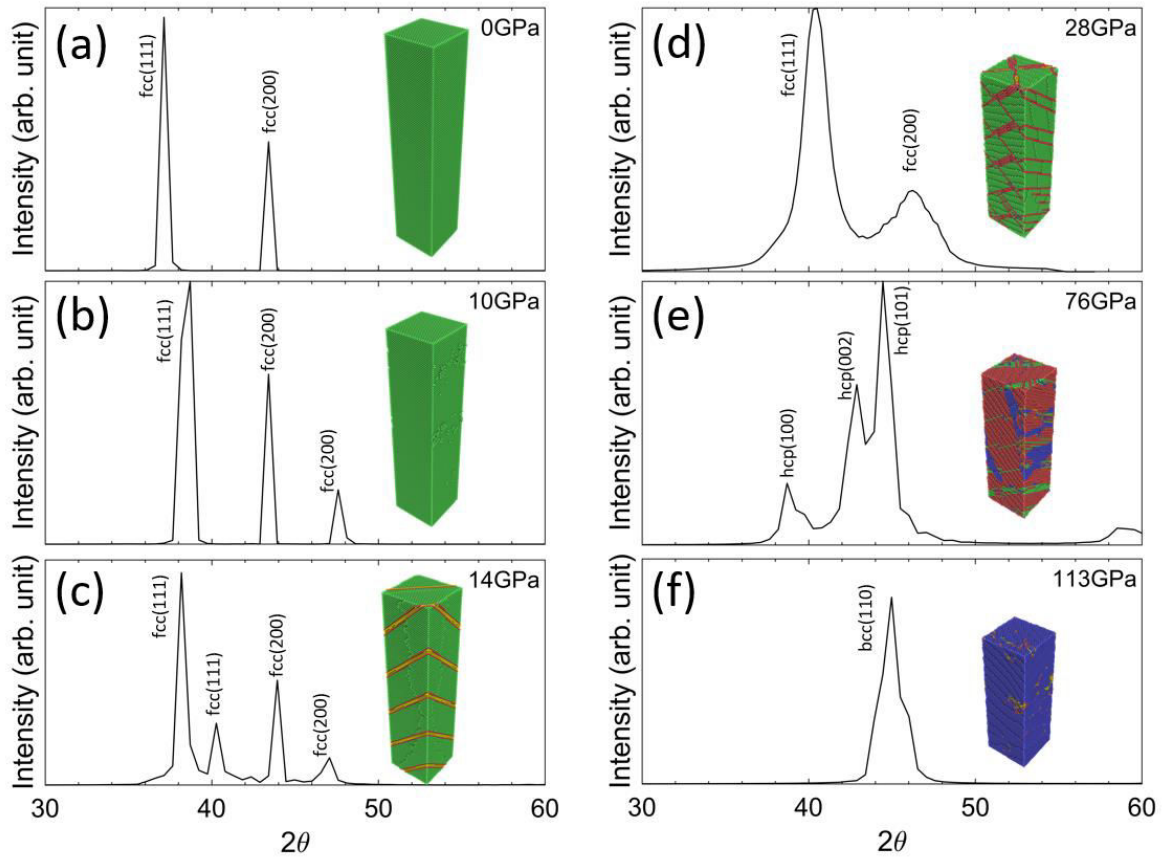


Figure 3 X-ray diffraction patterns for a representative slice (atomistic snapshots shown on the right and colored in the same manner as Fig. 2) from setup II at different stress state.

2. Characterization of ramp-loaded Al Microstructures using Virtual Diffraction

This section will discuss the applicability of using virtual diffraction to augment the characterization of the dislocation activity, twinning activity, and phase transformation. The virtual diffraction also allows for direct comparison between simulation and experimental results. Understanding the diffraction signature and establishing its corresponding relation to the atomistic picture will help in revealing the mechanisms of phase transformation from the *in-situ* diffractogram acquired during experiments. The characterization of the virtual XRD for the single-crystal structure is considered here. We take the snapshots of a representative slab, which has a length of 50 nm at 0 GPa, as illustrated in the insets of figure 3, and characterize this region using virtual XRD as it undergoes different elastic/plastic stages under the ramp loading.

The snapshot at 0 ps represents the initial unstrained, equilibrated microstructure. As shown in figure 3 (a), the XRD pattern for this snapshot demonstrates sharp peaks. The diffraction angle (2θ angle) for the first and second peaks of the XRD profile occurs at 37.13 degrees and 43.41 degrees, matching the reported value of the $\{111\}$ and $\{200\}$ peaks of fcc Al. As the ramp loading starts, the uniaxial compression along the $[001]$ direction will cause the (002) and $(00\bar{2})$ peaks shifting to larger angle, while the (200) , $(\bar{2}00)$, (020) , $(0\bar{2}0)$ peaks remain unchanged. This difference in straining of $\{200\}$ planes results in the splitting of the $\{200\}$ peak at 10 GPa, as shown in Figure 3 (b). On the contrary, all $\{111\}$ planes have the same angle with the loading direction and are thus compressed in the same magnitude, which results in the $\{111\}$ peak shifted to a larger angle instead of splitting. Starting from 14 GPa, we begin to see micro twin formation in the region along with the (111) planes. Interestingly, a splitting of the $\{111\}$ peaks is also observed associated with the occurrences of the micro twins. The splitting is due to the micro twins not only accommodating a significant amount of atomic strain but also allowing the elastic strain in the fcc phase to be redistributed in a non-uniform manner. Closer inspection of

the atomic picture reveals the (111), $(\bar{1}11)$, and $(\bar{1}\bar{1}\bar{1})$ planes remained unstrained. This corresponds to part of the first peak with no shifting from 10 GPa to 14 GPa; on the contrary, the $(\bar{1}\bar{1}\bar{1})$ plane is now more compressed with a new inter-plane distance of 2.15 Angstrom instead of 2.26 Angstrom, which corresponds to the split of the {111} peak where its second part occurred at a higher diffraction angle (second peak in the XRD). As stated in the previous section, starting at 17 GPa, new SFs along with the $(\bar{1}\bar{1}\bar{1})$ slip planes also start to nucleate and unzip the (111) micro twins into (111) SFs when coming into contact. Then at 28 GPa, the splitted {111} peaks recombined into one single peak, suggesting all {111} peaks are compressed at the same magnitude, and homogeneous straining in the fcc matrix is achieved again. In the meanwhile, significant broadening of the (111) and (200) peak is observed. More interestingly, there exists a discrepancy between the lattice constant calculated from the (111) peak (3.70 Å) and (200) peak (3.77 Å), suggesting the two peaks have shifted relatively. Sharma et al.²⁰ have investigated similar XRD profiles obtained during ramp compression of gold based on the theoretical work of Warren²¹ and concluded that the relative shifting of the peaks could only be due to the presence of SFs while broadening could be related to multiple mechanisms, including SFs, twinning, size broadening, and strain broadening. Thus, the existence of SFs in the structure can also be concluded from the 28 GPa XRD profile besides its corresponding atomistic configuration. As the strain goes on, the (111) stacking faults continue to thicken in certain parts of the structure. The thickened SFs have an hcp configuration with its basal planes $(001)_{\text{hcp}}$ parallel to $(111)_{\text{fcc}}$ slip planes. The XRD profile for this specific snapshot also exhibits hcp signature, as illustrated in Figure 3 (e). It is also noticed that even at the peak of the SFs thickening event (at around 76 GPa), only 41.2% of the total atoms are part of the SFs. This agrees with the observation that SFs thickening is not uniform in the structure. Then within 15

GPa, phase transformation becomes dominant and surpasses the SFs thickening globally. At 113

GPa, the bcc phase propagates across the entire structure, leading to an XRD profile exhibiting

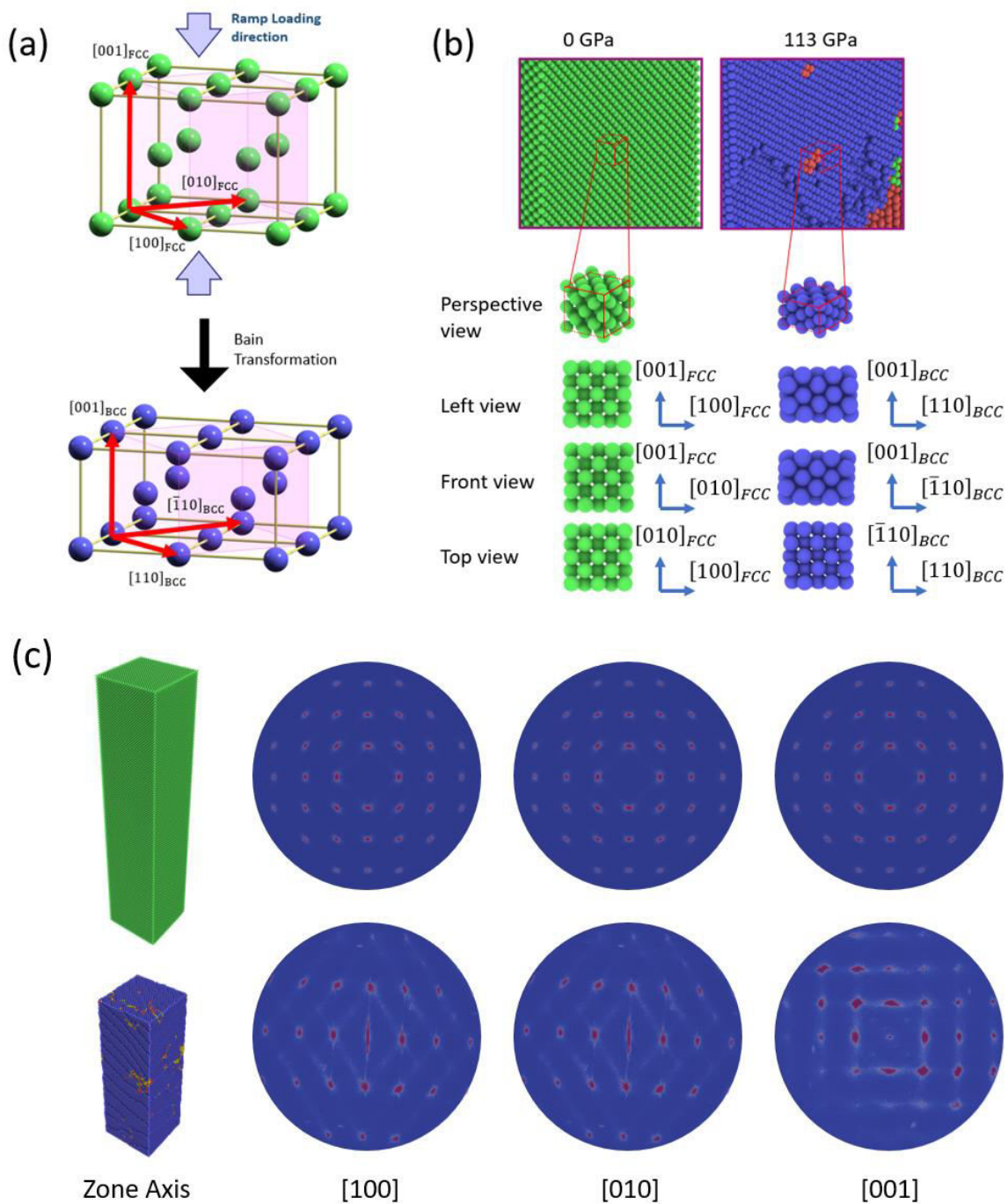


Figure 4 (a) Schematic of the Bain transformation (b) Perspective, left, front and top views of a supercell that undergoes a structural phase transformation during loading at different stress and the corresponding lattice orientation (c) SAED patterns for different zone Axis for a representative slice at 0 and 113 GPa.

the bcc Al signature.

3. Phase transformation path and comparison between simulation and experiments.

As stated in section 1, our simulations show a structural phase transformation from fcc to bcc under ramp compression. We further use polyhedral template matching to analyze the lattice orientation of the atoms. At 0 GPa, all FCC atoms have [100], [010], and [001] orientation along x, y, and z, respectively; at 113 GPa, all bcc atoms have [110], $[\bar{1}10]$, and [001] orientation along x, y, and z, respectively. Virtual SAED analysis (Figure 4 (c)) has also been carried out at these stresses and confirms these lattice orientations. These specific lattice orientations correspond to the Bain orientation relationship (OR)²² between the fcc and bcc phase, as illustrated in Figure 4 (a). The orientation relationship of a supercell that goes through Bain is shown in figure 4b. The virtual XRD patterns of the 0 GPa, 76GPa, and 399 GPa are also plotted against the experimental *in-situ* XRD took at 0 GPa, 291 GPa and 466 GPa, as shown in figure 5 (a) to (c). The fcc and bcc signature between experiment and simulation exhibited remarkable agreement. The lattice constant of bcc can be consequently calculated through the peak locations of figure 5 (c) to be around 2.43 Å at 466 GPa for the experiment and 2.33 Å at 399 GPa for the simulation. The experiments used a polycrystalline aluminum foil that had a strong initial texture, with all grains are (001)-orientated along the fiber axis. As illustrated in figure 5 (d) to (f), during the deformation, the $(111)_{\text{fcc}}$, $(002)_{\text{hcp}}$, $(011)_{\text{bcc}}$ spots are in close vicinity: angles between sample normal (i.e., fiber axis) and diffraction plane normal are all within 40°-60°. Thus it can be concluded from these figures that the $(111)_{\text{fcc}}$, $(002)_{\text{hcp}}$, $(011)_{\text{bcc}}$ spots are the same most close-packed planes that essentially remain parallel through the transformations. If we consider the thickened SFs as an hcp phase, their basal plane $(002)_{\text{hcp}}$ are parallel to $(111)_{\text{fcc}}$, which means the

normals to the $(002)_{\text{hcp}}$ planes make angles of 54.7° to the fiber axis. After the Bain transformation, we have $(011)_{\text{bcc}}$ parallel to $(111)_{\text{fcc}}$ and angles of 45° between the normal to $(011)_{\text{bcc}}$ and the fiber axis. To be noted, this only applies to $(011)_{\text{bcc}}$, $(0\bar{1}1)_{\text{bcc}}$, $(101)_{\text{bcc}}$, $(10\bar{1})_{\text{bcc}}$, while $(110)_{\text{bcc}}$ and $(\bar{1}10)_{\text{bcc}}$ are perpendicular to the fiber axis. These orientation analyses suggest that the phase transformation observed in the simulation matches that in the experiment. However, we can not directly compare the XRD patterns for the hcp phase from simulations and experiments. The simulated XRD profile is taken at 76 GPa. In comparison, the experimental XRD is taken at 291 GPa, which could explain why the peaks in the simulated profile are to the left of the experimental profile in Figure 5 (b). The mismatch is associated with the lower transition pressures for fcc-hcp and hcp-bcc phase transformation predicted by our simulations compared to experiments. This could be due to advanced growth and shortened persistence of the stacking faults in the NEMD simulations, which are based on small (scaling factor 1/20 vs. 1) cells and a slightly different boundary (rigid piston vs. LiF) in comparison to samples in the actual experiments, where the effect of nucleation dynamics could extend for microns²³. In addition, the periodic boundary conditions imposed on the lateral directions create elevated lateral stresses (at levels around 80% of the concurrent longitudinal stresses). Thus, the overall hydrostatic pressure in the simulation is much higher than that of the experiment. It has been shown that hydrostatic pressure favors transformations that are in a negative volumetric change and could trigger phase transformation on lower tensile stress levels²⁴. Further research on nucleation dynamics within solids and larger-scale billion-atom NEMD simulations will be beneficial in elucidating such discrepancies.

4. Plasticity Contributor in Texturized Nanocrystalline Al

An $\langle 001 \rangle_{\text{fcc}}$ -oriented texturized NC Al was used in the ramp loading experiment instead of the single-crystal. Thus, to investigate the effect of the grain boundaries on the resultant plastic deformation behaviors, we performed atomistic ramp loading simulations on $\langle 001 \rangle_{\text{fcc}}$ -oriented texturized NC Al structure with similar setups to SC structures. The lateral dimensions of the texturized NC Al are three times larger than the SC in order to accommodate grains of the size of

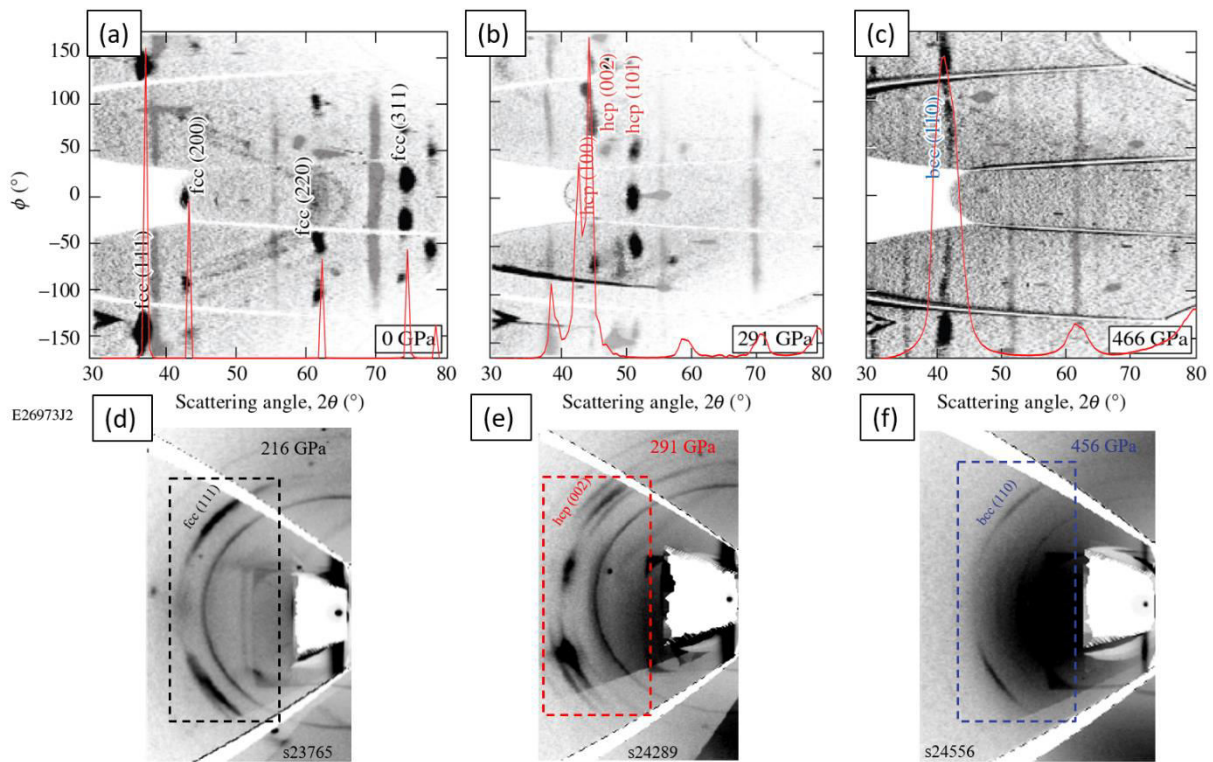


Figure 5 (a) to (c) Experiment and virtual XRD data taken at different stage of the ramp loading. The experimental data are taken at 0 GPa, 291 GPa and 466 GPa respectively. The virtual XRD data are taken at 0 GPa, 76 GPa and 399 GPa respectively. Notice the single crystal diffraction Laue spots from the diamond and LiF ablator/window plates are also presented and artificially dimmed to highlight Al diffraction signature. (d) to (f) Stereographic projection of the diffraction data from experiment taken at different stress. The black, red, and blue boxes enclose the Debye-Scherrer rings for the fcc (111), hcp (002), and bcc (110) planes, respectively. The evolution of the initial $[100]$ fiber texture is compared to these atomistic simulations.

15nm. As a result, the 100 nm length (scaling factor 1/200) might not exactly reflect the deformation behavior of systems with larger scaling factors, as discussed earlier in section 3. On the other hand, any difference between the texturized NC Al and the SC structures setup I (with a scaling factor of 1/200) can be attributed to the effect of grain boundaries, and comparing them allows us to understand the effect of grain boundaries in general.

The stress-strain curve for the texturized NC Al is shown in Figure 1 and exhibits a remarkable agreement to the experiments and setups I to III. Snapshots of the texturized NC Al at several critical pressures are shown in Figure 6 (a)-(e); it can be seen from the 14 and 28 GPa snapshot that the early plasticity is dominated by SFs rather than micro twins. The phase transformation also initiated and finished at smaller stresses; the entire structures transformed to bcc at 76 GPa, comparing to 113 GPa for setup II. Defect growth in the bcc phase is also initiated as soon as the phase transformation is completed, as illustrated by Figure 6 (e). All these observations are

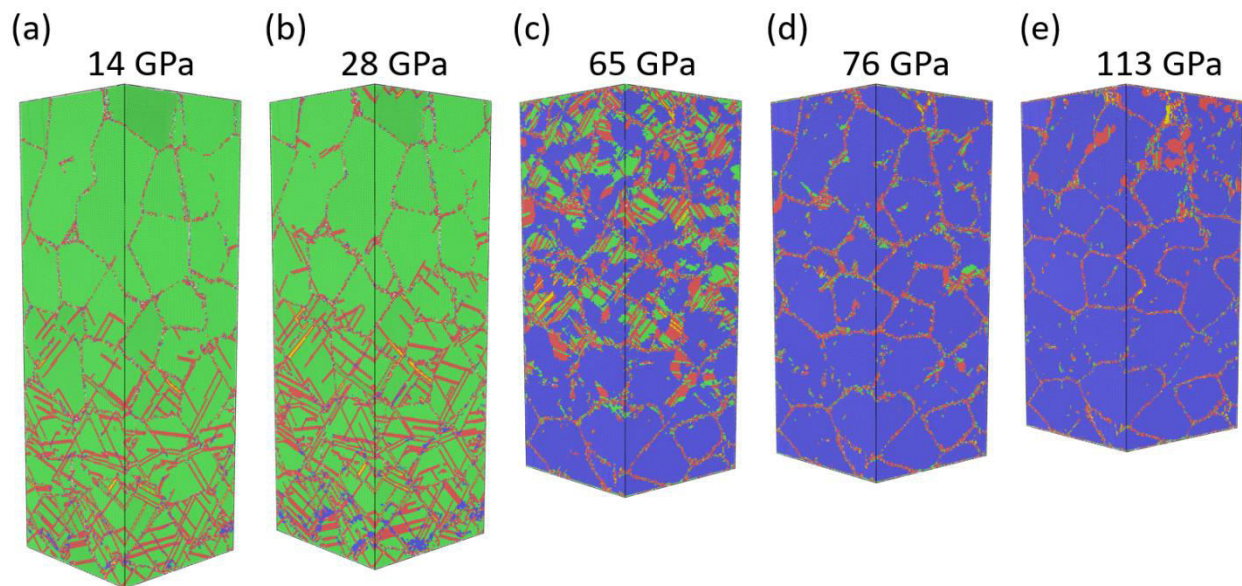


Figure 6 Atomistic snapshot of the texturized NC Al at different global stress. Atoms are colored in the same manner as Fig. 2. The loading direction is from bottom to top.

identical to setup I, which uses the same temporal and spatial scaling factors, suggesting the grain boundary has little effect on the ramp loading behavior. This finding is consistent with a recent study on the Hugoniot equation of state of Al²⁵. Interestingly, we note that previous experiments have shown insensitivity of the Hugoniot to the grain size and orientation of copper²⁶, whereas the dependence on the form of the crystal/sample is strong for diamond²⁷, silicon carbide²⁸, and TATB²⁹. This clearly implies different mechanisms in the response of different materials to dynamic compression that are likely closely related to their metallicity.

Conclusion

In conclusion, a series of NEMD simulations are carried out to investigate the plastic deformation properties of Al under ramp loading conditions. Setups with varying lengths and simulation time demonstrated a scaling approach is viable when the temporal and spatial parameters are scaled identically, and structure length is adequately long. An excellent agreement is observed in stress-density response between previously published laser-driven ramp compression experiments and simulation setups with proper scaling factors. Furthermore, the atomistic pictures and virtual diffraction analysis demonstrated a plastic deformation route of micro twin formation -> SFs formation -> SFs thickening -> phase transformation via Bain path. Finally, the virtual XRD patterns are compared with experimental in-situ XRD results and showed remarkable similarity in the fcc and bcc signature at comparable stress. The proposed phase transformation path is also cross-examined with the experimental diffraction result and showed perfect agreement. This study provided concrete evidence of the exact phase transformation path for Al taken place during ramp loading and also provided insights into

understanding experimental diffraction results by correlating the analysis of the virtual diffraction patterns with atomistic pictures.

Methods

The NEMD simulations are carried out using the Large-scale Atomic/Molecular Massively Parallel Simulator (LAMMPS)³⁰ code. The interactions between Al atoms are modeled using the embedded atom method (EAM) potential developed by Winey et al.³¹, which was specifically developed to investigate the high-pressure physics of Al and is widely used in shock-related simulation^{7, 32-34}. Specifically, Yang et al.²⁵ have used Winey potential to reproduce the Hugoniot curves, Grüneisen coefficient, and melting temperature of Al under shock loading up to 300 GPa and found great agreements with experiments. Before the loading, all structures underwent energy minimization using the conjugate gradient method with a maximum force tolerance of 10^{-27} eV/Å. Then two relaxation runs are carried out, first under zero pressure and room temperature in a Nosé–Hoover isothermal–isobaric (NPT) ensemble and then in a constrained energy and volume (NVE) ensemble. OVITO³⁵ is employed for post-processing of the simulation results and for the visualization of atomistic snapshots; Polyhedral Template Matching³⁶ is used for crystal structure and orientation identification; Dislocation Extraction Algorithm (DXA)³⁷ tool is used for dislocation analysis; Virtual X-ray diffraction (XRD) and Selected area electron diffraction (SAED)¹² implemented in LAMMPS are employed to generate diffraction signature of the atomistic snapshot at any given time. The virtual SAED irradiation wavelength is set at 0.0251 Å to mimic 200-keV electron radiation and is visualized using Paraview³⁸. The virtual XRD irradiation wavelength is set at either 1.48 Å or 1.21 Å to compare with the experiments (8.37-keV (Cu) and 10.25-keV (Ge) He- α) directly.

1. Fowles, G. R.; Duvall, G. E.; Asay, J.; Bellamy, P.; Feistmann, F.; Grady, D.; Michaels, T.; Mitchell, R., Gas Gun for Impact Studies. *Review of Scientific Instruments* **1970**, *41* (7), 984-996.
2. Weihua, J.; Yatsui, K.; Takayama, K.; Akemoto, M.; Nakamura, E.; Shimizu, N.; Tokuchi, A.; Rukin, S.; Tarasenko, V.; Panchenko, A., Compact solid-State switched pulsed power and its applications. *Proceedings of the IEEE* **2004**, *92* (7), 1180-1196.
3. Gizzi, L. A.; Koester, P.; Labate, L.; Mathieu, F.; Mazzotta, Z.; Toci, G.; Vannini, M., A viable laser driver for a user plasma accelerator. *Nuclear Instruments and Methods in Physics Research Section A: Accelerators, Spectrometers, Detectors and Associated Equipment* **2018**, *909*, 58-66.
4. Rygg, J. R.; Eggert, J. H.; Lazicki, A. E.; Coppari, F.; Hawreliak, J. A.; Hicks, D. G.; Smith, R. F.; Sorce, C. M.; Uphaus, T. M.; Yaakobi, B.; Collins, G. W., Powder diffraction from solids in the terapascal regime. *Review of Scientific Instruments* **2012**, *83* (11), 113904.
5. Celliers, P. M.; Bradley, D. K.; Collins, G. W.; Hicks, D. G.; Boehly, T. R.; Armstrong, W. J., Line-imaging velocimeter for shock diagnostics at the OMEGA laser facility. *Review of Scientific Instruments* **2004**, *75* (11), 4916-4929.
6. Polsin, D. N.; Fratanduono, D. E.; Rygg, J. R.; Lazicki, A.; Smith, R. F.; Eggert, J. H.; Gregor, M. C.; Henderson, B. J.; Gong, X.; Delettrez, J. A.; Kraus, R. G.; Celliers, P. M.; Coppari, F.; Swift, D. C.; McCoy, C. A.; Seagle, C. T.; Davis, J. P.; Burns, S. J.; Collins, G. W.; Boehly, T. R., X-ray diffraction of ramp-compressed aluminum to 475 GPa. *Physics of Plasmas* **2018**, *25* (8), 082709.
7. Liao, Y.; Xiang, M.; Zeng, X.; Chen, J., Molecular dynamics studies of the roles of microstructure and thermal effects in spallation of aluminum. *Mechanics of Materials* **2015**, *84*, 12-27.
8. Neogi, A.; He, L.; Abdolrahim, N., Atomistic simulations of shock compression of single crystal and core-shell Cu@Ni nanoporous metals. *Journal of Applied Physics* **2019**, *126* (1), 015901.
9. Lane, J. M. D.; Foiles, S. M.; Lim, H.; Brown, J. L., Strain-rate dependence of ramp-wave evolution and strength in tantalum. *Physical Review B* **2016**, *94* (6), 064301.
10. Akahama, Y.; Nishimura, M.; Kinoshita, K.; Kawamura, H.; Ohishi, Y., Evidence of a fcc-hcp Transition in Aluminum at Multimegabar Pressure. *Physical Review Letters* **2006**, *96* (4), 045505.

11. Mattsson, T. K. R.; Desjarlais, M. P.; Grest, G. S.; Templeton, J. A.; Thompson, A. P.; Jones, R. E.; Zimmerman, J. A.; Baskes, M. I.; Winey, J. M.; Gupta, Y. M.; Lane, J. M. D.; Ditmire, T.; Quevedo, H. J. *Modeling ramp compression experiments using large-scale molecular dynamics simulation*; United States, 2011-10-01, 2011.
12. Coleman, S. P.; Spearot, D. E.; Capolungo, L., Virtual diffraction analysis of Ni [0 1 0] symmetric tilt grain boundaries. *Modelling and Simulation in Materials Science and Engineering* **2013**, *21* (5), 055020.
13. Polsin, D. N.; Fratanduono, D. E.; Rygg, J. R.; Lazicki, A.; Smith, R. F.; Eggert, J. H.; Gregor, M. C.; Henderson, B. H.; Deletrez, J. A.; Kraus, R. G.; Celliers, P. M.; Coppari, F.; Swift, D. C.; McCoy, C. A.; Seagle, C. T.; Davis, J. P.; Burns, S. J.; Collins, G. W.; Boehly, T. R., Measurement of Body-Centered-Cubic Aluminum at 475 GPa. *Physical Review Letters* **2017**, *119* (17), 175702.
14. Cui, Z.; Gao, F.; Cui, Z.; Qu, J., A second nearest-neighbor embedded atom method interatomic potential for Li-Si alloys. *Journal of Power Sources* **2012**, *207*, 150-159.
15. Falco, S.; Jiang, J.; De Cola, F.; Petrinic, N., Generation of 3D polycrystalline microstructures with a conditioned Laguerre-Voronoi tessellation technique. *Computational Materials Science* **2017**, *136*, 20-28.
16. Olson, G. B.; Cohen, M., A mechanism for the strain-induced nucleation of martensitic transformations. *Journal of the Less Common Metals* **1972**, *28* (1), 107-118.
17. Acelrad, O.; Kalashnikov, I. S.; Silva, E. M.; Khadyev, M. S.; Simao, R. A., Diagram of phase transformations in the austenite of hardened alloy Fe-28% Mn-8.5% Al-1% C-1.25% Si as a result of aging due to isothermal heating. *Metal Science and Heat Treatment* **2006**, *48* (11), 543-553.
18. Božić, B. I.; Lučić, R. J., Martensitic transformation in iron-arsenic alloys. *Journal of Materials Science* **1977**, *12* (4), 751-756.
19. Nagy, E.; Mertinger, V.; Tranta, F.; Sólyom, J., Deformation induced martensitic transformation in stainless steels. *Materials Science and Engineering: A* **2004**, *378* (1), 308-313.
20. Sharma, S. M.; Turneaure, S. J.; Winey, J. M.; Rigg, P. A.; Sinclair, N.; Wang, X.; Toyoda, Y.; Gupta, Y. M., Real-Time Observation of Stacking Faults in Gold Shock Compressed to 150 GPa. *Physical Review X* **2020**, *10* (1), 011010.
21. Warren, B. E.; Warekois, E. P., Measurements of Stacking Faults in Cold - Worked Alpha Brass. *Journal of Applied Physics* **1953**, *24* (7), 951-952.
22. Bain, E. C., The Nature of Martensite. *Trans. AIME Steel Division* **1924**, *79*, 25.
23. Budzevich, M. M.; Zhakhovsky, V. V.; White, C. T.; Oleynik, I. I., Evolution of Shock-Induced Orientation-Dependent Metastable States in Crystalline Aluminum. *Physical Review Letters* **2012**, *109* (12), 125505.
24. Jacobus, K.; Sehitoglu, H.; Balzer, M., Effect of stress state on the stress-induced martensitic transformation in polycrystalline Ni-Ti alloy. *Metallurgical and Materials Transactions A* **1996**, *27* (10), 3066-3073.
25. Yang, X.; Zeng, X.; Pu, C.; Chen, W.; Chen, H.; Wang, F., Molecular dynamics modeling of the Hugoniot states of aluminum. *AIP Advances* **2018**, *8* (10), 105212.
26. Chau, R.; Stölken, J.; Asoka-Kumar, P.; Kumar, M.; Holmes, N. C., Shock Hugoniot of single crystal copper. *Journal of Applied Physics* **2010**, *107* (2), 023506.

27. Gregor, M. C.; Fratanduono, D. E.; McCoy, C. A.; Polsin, D. N.; Sorce, A.; Rygg, J. R.; Collins, G. W.; Braun, T.; Celliers, P. M.; Eggert, J. H.; Meyerhofer, D. D.; Boehly, T. R., Hugoniot and release measurements in diamond shocked up to 26 Mbar. *Physical Review B* **2017**, *95* (14), 144114.
28. Li, W.; Hahn, E. N.; Yao, X.; Germann, T. C.; Feng, B.; Zhang, X., On the grain size dependence of shock responses in nanocrystalline sic ceramics at high strain rates. *Acta Mater* **2020**, *200*, 632-651.
29. Marshall, M. C.; Fernandez-Pañella, A.; Myers, T. W.; Eggert, J. H.; Erskine, D. J.; Bastea, S.; Fried, L. E.; Leininger, L. D., Shock Hugoniot measurements of single-crystal 1,3,5-triamino-2,4,6-trinitrobenzene (TATB) compressed to 83 GPa. *Journal of Applied Physics* **2020**, *127* (18), 185901.
30. Plimpton, S., Fast Parallel Algorithms for Short-Range Molecular Dynamics. *Journal of Computational Physics* **1995**, *117* (1), 1-19.
31. Winey, J. M.; Kubota, A.; Gupta, Y. M., A thermodynamic approach to determine accurate potentials for molecular dynamics simulations: thermoelastic response of aluminum. *Modelling and Simulation in Materials Science and Engineering* **2009**, *17* (5), 055004.
32. Xiang, M.; Cui, J.; Yang, Y.; Liao, Y.; Wang, K.; Chen, Y.; Chen, J., Shock responses of nanoporous aluminum by molecular dynamics simulations. *International Journal of Plasticity* **2017**, *97*, 24-45.
33. Xue, S.; Fan, Z.; Lawal, O. B.; Thevamaran, R.; Li, Q.; Liu, Y.; Yu, K. Y.; Wang, J.; Thomas, E. L.; Wang, H.; Zhang, X., High-velocity projectile impact induced 9R phase in ultrafine-grained aluminium. *Nature Communications* **2017**, *8* (1), 1653.
34. Zimmerman, J. A.; Winey, J. M.; Gupta, Y. M., Elastic anisotropy of shocked aluminum single crystals: Use of molecular dynamics simulations. *Physical Review B* **2011**, *83* (18), 184113.
35. Alexander, S., Visualization and analysis of atomistic simulation data with OVITO—the Open Visualization Tool. *Modelling and Simulation in Materials Science and Engineering* **2010**, *18* (1), 015012.
36. Larsen, P. M.; Schmidt, S.; Schiøtz, J., Robust structural identification via polyhedral template matching. *Modelling and Simulation in Materials Science and Engineering* **2016**, *24* (5), 055007.
37. Stukowski, A.; Bulatov, V. V.; Arsenlis, A., Automated identification and indexing of dislocations in crystal interfaces. *Modelling and Simulation in Materials Science and Engineering* **2012**, *20* (8), 085007.
38. Ayachit, U., *The ParaView Guide: A Parallel Visualization Application*. Kitware, Inc.: 2015.

Acknowledgements

This study was supported by the U.S. Department of Energy, Office of Science, Fusion Energy Sciences under Award Number DE-SC0020340.

Author contributions

L.H, and N.A conceived and designed the study; D.P., S. Z., and G.W.C. performed the experiment. L.H and N.A conducted the simulation and analyzed the data. L.H, N.A, D,P and S.Z. wrote the paper. All authors reviewed the manuscript.

Competing interests

The authors declare no competing interests.